

Received November 8, 2018, accepted December 4, 2018, date of publication December 7, 2018, date of current version December 31, 2018.

Digital Object Identifier 10.1109/ACCESS.2018.2885514

# A Novel Total Variation Model for Low-Dose CT Image Denoising

WENBIN CHEN<sup>1</sup>, YANLING SHAO<sup>2</sup>, YANLING WANG<sup>3</sup>, QUAN ZHANG<sup>1</sup>, YI LIU<sup>1</sup>, LINHONG YAO<sup>2</sup>, YAN CHEN<sup>1</sup>, GUANRU YANG<sup>4</sup>, AND ZHIGUO GUI<sup>1</sup>

<sup>1</sup>Shanxi Provincial Key Laboratory for Biomedical Imaging and Big Data, North University of China, Taiyuan 030051, China

<sup>2</sup>School of Science, North University of China, Taiyuan 030051, China

<sup>3</sup>School of Information Management, Shanxi University of Finance and Economics, Taiyuan 030006, China

<sup>4</sup>School of Information and Communications Engineering, Beijing University of Technology, Beijing 100124, China

Corresponding author: Zhiguo Gui (gzgtg@163.com)

This work was supported in part by the National Key Scientific Instrument and Equipment Development Project of China under Grant 2014YQ24044508, in part by the National Natural Science Foundation of China under Grant 61671413, and in part by the National Natural Science Foundation of China under Grant 61801438.

**ABSTRACT** Low-dose computed tomography (LDCT) images are polluted by mottle noise and streak artifacts. To improve LDCT images quality, this paper proposes a novel total variation (NTV) model. A weighted coefficient of the regularization term of NTV model is constructed by standard deviation, gray-level probability and gradient magnitude to smooth LDCT images adaptively, since the standard deviation and the gray-level probability of detail region are higher than that of the noisy background, and the gradient magnitude of edges is higher than that of the noisy background. Besides, to preserve details and edges effectively, the fidelity term of the proposed NTV model is constructed by the block-matching 3d filter because it performs well in details and edges preservation. The experiments are performed on the computer simulated phantom and the actual phantom. Compared with several other competitive methods, both subjective visual effect and objective evaluation criteria show that the proposed NTV model can improve LDCT images quality more effectively such as noise and artifacts suppression, details, and edges preservation.

**INDEX TERMS** Low-dose CT, image denoising, total variation, weighted coefficient, edges and details preservation.

## I. INTRODUCTION

X-ray Computed Tomography (CT) has been widely used in clinical diagnosis and therapy since it was put forward in the 1970s. CT technology provides high resolution medical sectional anatomy images compared with other radiological examinations, but patients receive high radiation doses during CT examinations [1]. High radiation doses can lead to increased likelihood of the incidence of genetic disease and cancer, and radiation doses in the body of patients accumulate with age [2]. So, controlling radiation doses and getting LDCT images are of great significance to patients. Radiation doses are determined by many scanning parameters, such as scanner geometry, tube current and voltage, scanning modes, and so on [3]. Correspondingly, there are many methods to reduce radiation doses, among which, lowering tube current is the most commonly used, nevertheless, the reconstructed LDCT images by this way are badly damaged by mottle noise

and streak artifacts [4]. Based on this, many approaches have been put forward to improve the quality of LDCT images. Usually these approaches are divided into three categories: projection-data-processing approaches, iterative reconstruction approaches and post-processing approaches.

In projection-data-processing approaches, projection data are preprocessed, and then the reconstructed images are obtained from the processed projection data by classical filtered back projection (FBP) algorithm. A lot of researches have been done on this category. Multiscale least-square filter [5], bilateral filter [6], statistic-based iterative filter [7], fuzzy-median filter [8], and total generalized variation filter [9] were proposed to remove noise in projection data respectively. The disadvantage of this category is that it is difficult to get raw projection data. Unlike projection-data-processing approaches, the main goal of the iterative reconstruction approaches is to find the optimal solution

of the objective function with a priori regularization term concerned with the noise characteristics of projection data. Different priori terms will lead to different reconstruction results. Therefore, the key is to construct effective priori terms. So far, a lot of priori terms have been constructed, such as the total variation priors [10], [11], the non-local means priors [12], [13], the compressed sensing prior [14], and the dictionary learning prior [15]. Unfortunately, the process of iterative reconstruction approaches always needs much time.

The third one, i.e., post-processing approaches, does not rely on raw projection data and can be applied to different scanning systems. In the past decade, a variety of post-processing approaches were proposed, such as bilateral filter and nonlocal means [16], a weighted intensity averaging over large-scale neighborhoods filter [17], a large-scale nonlocal means (LNLM) filter combined with a multiscale directional diffusion scheme [18], an artifact suppressed dictionary learning approach [19], an approach of deep convolutional neural network [20], a penalized weighted least-squares (PWLS) algorithm [21], and a filter based on fractional-order partial differential equations, i.e., FPMTV model [22].

During the last two decades, partial differential equations (PDEs) have been developed as effective tools for image denoising and they are widely used in post-processing approaches. Among them, the PM model proposed by Perona and Malik [23] and the total variation (TV) model proposed by Rudin, Osher, and Fatemi [24] perform well in noise removing, but they suffer from blocky effect seriously. It is visually unpleasant and mistakenly identified as edges in the smooth area. To solve this problem, some high-order PDEs were proposed for image denoising. For example, one of the most popular four-order PDEs, YK model, was introduced by You and Kaveh [25], and the other two classical four-order PDEs models were proposed by Lysaker, Lundervold and Tai (LLT model) [26] and Mohammad Reza Hajiaboli (MRH model) [27] respectively. Although these fourth-order models do not cause blocky effect, speckle noise exists in the filtered image.

Besides, to reduce blocky effect, the modified total variation (MTV) [28] model was also proposed and it can reduce blocky effect to a certain degree, but there are still two deficiencies: ① The regularization term of MTV model is not spatially smoothing adaptive. ② In addition, the MTV model uses Gaussian operator to construct the fidelity term, which makes the model not conducive to edges and details preservation, because the Gaussian filter blurs edges. Unlike local Gaussian filter, the BM3D model [29] is a patch-based model in nonlocal areas, and it has been proven to be superior to previous image denoising algorithms and shows outstanding performance in details and edges preservation. Therefore, in order to overcome these deficiencies of the MTV model, the NTV model is proposed in this paper by taking the advantage of BM3D filter. In NTV model, to achieve adaptive diffusion, the adaptive weighted coefficient of the regularization term is constructed by standard deviations, gray-level probability and gradient magnitude, since the standard deviation and the

gray-level probability can differentiate fine details from noisy background, and the gradient magnitude can differentiate edges from noisy background. Besides, instead of Gaussian filter used in the fidelity term of MTV model, the NTV model use BM3D filter to obtain the image in the fidelity term. Then, the NTV model is applied to LDCT images restoration.

The structure of this paper is as follows: in section 2, we briefly summarize the concepts of TV method, MTV model and BM3D algorithm firstly, then the NTV model is proposed and its numerical computation is discussed. Experimental results on LDCT images are given and discussed in section 3. Conclusions are sketched in section 4.

## II. MATERIALS AND METHODS

### A. RELATED WORKS

#### 1) TV MODEL

In general, images can be viewed as functions with discontinuities, so they are always assumed in the Bounded Variation (BV) space [30] since it allows discontinuities in functions. Based on which, the TV model, a variational model, was put forward. The definition of BV space is given as:

*Definition 1:* Let  $\Omega \subset \mathbb{R}^n$  be an open subset with Lipschitz boundary. The function  $u \in L^1(\Omega)$ . Define  $BV(\Omega)$  (BV) space as the subspace of functions  $u$  if the following inequality is true:

$$\int_{\Omega} |Du| = \sup \left\{ \int_{\Omega} u \operatorname{div} \varphi \, dx \mid \varphi \in C_c^1(\Omega; \mathbb{R}^n), |\varphi| \leq 1 \right\} < \infty,$$

where  $\int_{\Omega} |Du|$  stands for the total variation of  $u$ .

With the norm  $\|u\|_{BV(\Omega)} = \int_{\Omega} |Du| + \|u\|_{L^1(\Omega)}$ ,  $BV(\Omega)$  is a Banach space [31].

TV model can preserve edges well while removing noise by minimizing the following problem:

$$\min_u E(u) = \min_u \int_{\Omega} |\nabla u| \, d\Omega + \frac{\lambda}{2} \int_{\Omega} (u - I)^2 \, d\Omega, \quad (1)$$

where  $\Omega \subset \mathbb{R}^2$  denotes the image domain,  $\nabla$  is the gradient operator.  $\int_{\Omega} |\nabla u| \, d\Omega$  stands for the total variation of  $u$ .  $I(x, y)$  is the input noisy image that needs to be restored,  $u(x, y)$  is the restored image. The first term of the energy  $E(u)$  is the regularization term, and the second term is the fidelity term.  $\lambda$ , a positive weight parameter, is introduced to adjust the relative weight between the regularization term and the fidelity term.

In order to minimize energy function  $E(u)$ , we need to solve the associated Euler-Lagrange equation of (1). The corresponding Euler-Lagrange equation of (1) is:

$$\lambda(u - I) - \nabla \cdot \left( \frac{\nabla u}{|\nabla u|} \right) = 0 \quad (2)$$

The solution of (1) is usually achieved by the steepest descent method:

$$\frac{\partial u}{\partial t} = \nabla \cdot \left( \frac{\nabla u}{|\nabla u|_{\beta}} \right) - \lambda(u - I) \quad (3)$$

where,  $|\nabla u|_{\beta} = \sqrt{|\nabla u|^2 + \beta^2}$  is the regularization item of  $|\nabla u|$ ,  $\beta$  is the infinite decimal to avoid 0 denominator.

As an improvement on the TV model, the weighted TV ( $\alpha$ -TV) model was discussed in [32]. Instead of BV space, the  $\alpha$ -TV model is based on the weighted BV( $\alpha$ -BV) space [33], and the weighted regularization term in the  $\alpha$ -TV model can lead to spatially adaptive image restoration. The definition of  $\alpha$ -BV space is given as:

*Definition 2:* A function  $u \in L^1(\Omega)$  belongs to  $\alpha$ -BV space in  $\Omega$  if:

$$\int_{\Omega} \alpha |Du| = \sup \left\{ \int_{\Omega} u \operatorname{div} \varphi \, dx \mid \varphi \in C_c^1(\Omega; R^n), |\varphi| \leq \alpha \right\} < \infty,$$

where  $\alpha$  is a positive valued continuous function on  $R^n$ .

The  $\alpha$ -TV model is as follows:

$$\min_u E(u) = \min_u \int_{\Omega} \alpha |\nabla u| \, d\Omega + \frac{\lambda}{2} \int_{\Omega} (u - I)^2 \, d\Omega, \quad (4)$$

the weighted coefficient  $\alpha$  is larger away from possible edges and smaller near a likely edge. Hence the  $\alpha$ -TV model is more beneficial to edges preservation.

### 2) MTV MODEL

It is known that the TV model tends to yield a piecewise constant image, and thus can give rise to the staircase effect in smooth regions of the image. To reduce the staircase effect, by making use of the structure information of the input noisy image  $I(x, y)$ , the MTV [28] model was proposed. MTV model minimizes the variation of  $u(x, y)$  along the tangent direction of the isophotes of image  $I(x, y)$ , as follows:

$$\min_u E(u) = \min_u \int_{\Omega} \sqrt{|(u_x, u_y)(n_x, n_y)^T|} \, d\Omega + \frac{\lambda}{2} \int_{\Omega} (u - f)^2 \, d\Omega, \quad (5)$$

where,

$$(u_x, u_y) = \nabla u, \quad (n_x, n_y) = \left( \frac{-f_y}{\sqrt{f_x^2 + f_y^2}}, \frac{f_x}{\sqrt{f_x^2 + f_y^2}} \right), \\ (f_x, f_y) = \nabla f, \quad f = I_{Gaussian},$$

$I_{Gaussian}$  is the result image of  $I$  filtered by the Gaussian filter.

Using the steepest descent method, gradient flow equation is obtained as follows:

$$\frac{\partial u}{\partial t} = \frac{1}{\sqrt{|(u_x, u_y)(n_x, n_y)^T|}^3} \frac{u_{xx}f_y^2 - 2f_xf_yu_{xy} + u_{yy}f_x^2}{f_x^2 + f_y^2} - \lambda(u - f) \quad (6)$$

The MTV model performs better than the TV model in preserving edges while avoiding blocky effect and speckles noise, but there is still blocky effect.

### 3) BM3D MODEL

Another novel image denoising algorithm BM3D [29], based on sparse representation, appears to be the state of the art image restoration algorithm. Next, we recall here its two basic steps: get a basic estimate and get a final estimate of the true image. The basic estimate is obtained by means of

block-matching and hard-thresholding the coefficients of a 3D transform from the input noisy image. The final estimate is obtained from the basic estimate and by replacing the hard-thresholding with the Wiener filter, with the difference that block-matching also takes place on the basic estimate of the clean image.

## B. THE NTV MODEL

For the MTV model, the regularization term is not spatially adaptive, and the fidelity term constructed by the Gaussian filter is not conducive to edges and details preservation. Hence, inspired by the ideas [29] and [32], we propose a new algorithm, NTV model. In the new model, weighted regularization term and modified fidelity term are constructed to preserve edges and details adaptively.

### 1) STANDARD DEVIATION

Standard deviation reflects the dispersion degree of a data set. A low standard deviation indicates that the data tends to be close to the mean of the set, vice versa. In this paper, for a given pixel  $u(i, j)$  at coordinate  $(i, j)$ , the standard deviation is determined by its  $3 \times 3$  neighborhood, the computational formula is as follows:

$$D(i, j) = \operatorname{sqr}t\left(\frac{1}{3^2} \times \sum_{m=i-1}^{i+1} \sum_{n=j-1}^{j+1} (u_{mn} - \bar{u})^2\right).$$

### 2) GRAY-LEVEL PROBABILITY

The gray-level probability [34]  $P^{Rij}(i, j)$  is decided by its  $3 \times 3$  neighborhood region  $R_{ij}$ , defined as:

$$P^{Rij}(i, j) = \frac{u(i, j)}{u^R(i, j)},$$

where  $u^R(i, j)$  is the sum of the gray levels in the  $3 \times 3$  neighborhood region  $R_{ij}$ .

### 3) THE NTV MODEL

The NTV model proposed in this paper is also based on the weighted BV ( $\alpha$ -BV) space. Suppose that  $\Omega \subset R^2$  is an open subset with Lipschitz boundary. Given image  $I : \Omega \rightarrow R$  is a LDCT image, which is corrupted by mottle noise and streak artifacts. The proposed NTV model based on  $\alpha$ -BV space is supposed to restore the estimated image  $u$  from  $I$ , and it is described as follows:

$$\min_u E(u) = \min_u \int_{\Omega} \alpha \sqrt{|(u_x, u_y)(n_x, n_y)^T|} \, d\Omega + \frac{\lambda}{2} \int_{\Omega} (u - I_{BM3D})^2 \, d\Omega, \quad (7)$$

where  $(u_x, u_y), (n_x, n_y), (f_x, f_y), f$  are the same as those in equation (5).  $I_{BM3D}$  is the result image of  $I$  processed by BM3D filter.  $\lambda > 0$  is the weighted coefficient of the fidelity term.  $\alpha = \frac{1}{1 + \frac{(S_f \cdot P_f \cdot |\nabla f|)^2}{k}}$  is a positive spatially adaptive weighted coefficient of the regularization term, and it controls the amount of diffusion adaptively.  $k > 0$  is a parameter that

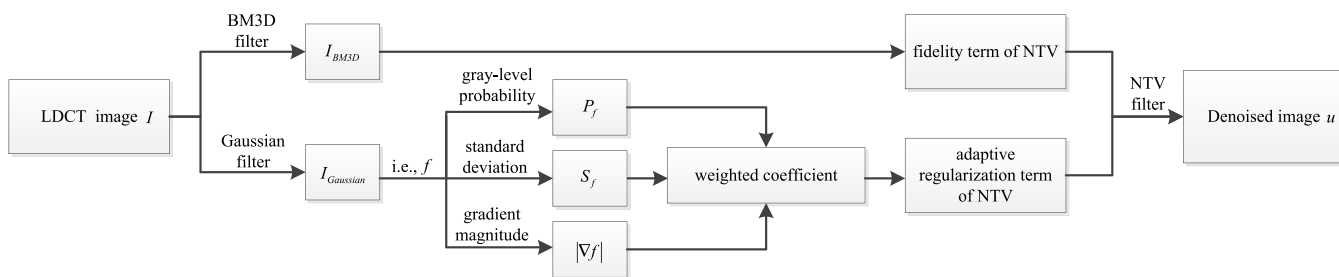


FIGURE 1. Flowchart of the proposed NTV model.

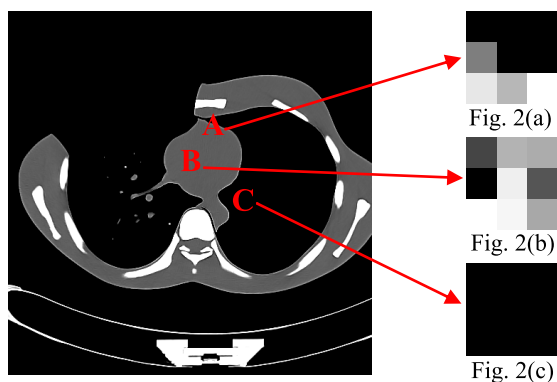


FIGURE 2. Three enlarged sub-images of the thoracic phantom. (a) a neighborhood of size  $3 \times 3$  centered around the pixel “A”; (b) a neighborhood of size  $3 \times 3$  centered around the pixel “B”; (c) a neighborhood of size  $3 \times 3$  centered around the pixel “C”.

determines the contrast of edges and details to be preserved,  $S_f$  is the standard deviation of  $f$ ,  $P_f$  is the gray-level probability of  $f$  and  $|\nabla f|$  is the gradient magnitude of  $f$ .

For a given  $k$ , the gradient magnitude  $|\nabla f|$  in the noisy background and the detail region is similar and smaller than that of edges, so it can't differentiate the detail region and the noisy background effectively. Therefore, the gray-level variance  $\sigma_f^2$  is introduced and it has been confirmed that the  $\sigma_f^2$  of detail region is larger than that of noisy background [35], accordingly, the square root of  $\sigma_f^2$ , i.e., the standard deviation  $\sigma_f$ , can also differentiate detail region and noisy background.

In addition, in [34], the gray-level probability was introduced into PM model and the revised model preserves not only edges but also fine details during smoothing process. In order to study the value of gray-level probability  $P_f$  in different regions, we choose pixels “A”, “B” and “C” from the thoracic phantom, as shown in Fig. 2. “A” represents the pixel in the edges, “B” represents the pixel in the detail region, and “C” represents the pixel in the noisy background. Fig. 2(a), Fig. 2(b) and Fig. 2(c) are the enlarged  $3 \times 3$  neighborhoods centered around the pixel “A”, “B” and “C” respectively. Table 1 shows the gray-level probability values of the pixel “A”, “B” and “C”. It indicates that the gray-level probability  $P_f$  of detail region is larger than that of edges and noisy background.

TABLE 1. The gray-level probability of pixels in different areas of the thoracic phantom.

pixel	gray-level probability
“A”	0.0358
“B”	0.1346
“C”	0

In summary, in the noisy background, standard deviation  $S_f$ , gray-level probability  $P_f$  and gradient magnitude  $|\nabla f|$  are all low, so  $\alpha$  is high, which allows strong diffusion, and the noise can be removed as much as possible. In the detail region, standard deviation  $S_f$  and gray-level probability  $P_f$  are both high, but gradient magnitude  $|\nabla f|$  is low, so  $\alpha$  is smaller than that in the noisy background and so that the details information can be preserved better. Beyond that, in the edges, gradient magnitude  $|\nabla f|$  and standard deviation  $S_f$  are both high, but gray-level probability  $P_f$  is low, so  $\alpha$  is also smaller than that in the noisy background and therefore the edges can also be well preserved. Base on the above, in order to preserve details and edges while removing noise and artifacts, the standard deviation  $S_f$ , the gray-level probability  $P_f$  and the gradient magnitude  $|\nabla f|$  are all used to construct the weighted coefficient  $\alpha$  of the proposed NTV model.

#### 4) NUMERICAL COMPUTATION

In this paper, the steepest descent method is applied to solve the optimization problem (7).

The steepest descent method is formulated as follows: In general, searching for the minimum of problem (7) is equivalent to solving its corresponding Euler-Lagrange equation. However, Euler-Lagrange equation is a static nonlinear partial differential equation, and it is hard to solve. By introducing time assistant variable  $t$ , solving the static nonlinear partial differential equation is changed into solving dynamic nonlinear partial differential equations. So, the key to solving the Euler-Lagrange equation corresponding to problem (7) is to obtain the steady evolution state of dynamic partial differential equations.

The corresponding Euler-Lagrange equation of (7) is:

$$\frac{\alpha(f_x^2 u_{yy} + f_y^2 u_{xx} - f_x f_y u_{xy} - f_x f_y u_{yx})}{4(f_x^2 + f_y^2)^{\frac{1}{4}}(f_x u_y - f_y u_x)^{\frac{3}{2}}} + \frac{\lambda(u - I_{BM3D})}{4} = 0 \quad (8)$$

with the initial condition  $u(x, 0) = I, x \in \Omega$ .

Numerically, the gradient descent flow (9) of (7) is obtained by the steepest descent method:

$$\frac{\partial u}{\partial t} = \frac{\alpha(-f_x f_y u_{xy} - f_x f_y u_{yx} + f_x^2 u_{yy} + f_y^2 u_{xx})}{4(f_x^2 + f_y^2)^{\frac{1}{4}}(f_x u_y - f_y u_x)^{\frac{3}{2}}} + \frac{\lambda(u - I_{BM3D})}{4} \quad (9)$$

In order to obtain the solution of (8), i.e., the stable solution of (9), it is necessary to make the following equation true:

$$\frac{\partial u}{\partial t} = 0 \quad (10)$$

Finite differences method is applied [24], [36] to discretize equation (9). Let  $\Delta x = 1$  and  $\Delta y = 1$  be the mesh sizes of variables  $x$  and  $y$ , and  $\Delta t$  be the time step. Suppose that  $u(x_i, y_j, t_k)$  is denoted by  $u_{i,j}^k$ , thus we have the following difference operations:

$$\begin{aligned} (f_{i,j}^k)_x &= \frac{f_{i+1,j}^k - f_{i-1,j}^k}{2}, & (f_{i,j}^k)_y &= \frac{f_{i,j+1}^k - f_{i,j-1}^k}{2}, \\ (u_{i,j}^k)_x &= \frac{u_{i+1,j}^k - u_{i-1,j}^k}{2}, & (u_{i,j}^k)_y &= \frac{u_{i,j+1}^k - u_{i,j-1}^k}{2}, \\ (u_{i,j}^k)_x^+ &= u_{i+1,j}^k - u_{i,j}^k, & (u_{i,j}^k)_y^+ &= u_{i,j+1}^k - u_{i,j}^k, \\ (u_{i,j}^k)_{xx} &= (u_{i,j}^k)_x^+ - (u_{i-1,j}^k)_x^+, & (u_{i,j}^k)_{yy} &= (u_{i,j}^k)_y^+ - (u_{i,j-1}^k)_y^+, \\ (u_{i,j}^k)_{xy} &= (u_{i,j}^k)_{yx} = \frac{(u_{i+1,j+1}^k + u_{i-1,j-1}^k - u_{i+1,j-1}^k - u_{i-1,j+1}^k)}{4}, \end{aligned}$$

So the iterative numerical solution of model (7) for pixel  $u_{i,j}$  on the  $k$ th iteration is described as below:

$$u_{i,j}^{k+1} = u_{i,j}^k + \Delta t \left( \frac{\alpha(-f_x f_y u_{xy} - f_x f_y u_{yx} + f_x^2 u_{yy} + f_y^2 u_{xx})}{4(f_x^2 + f_y^2)^{\frac{1}{4}}(f_x u_y - f_y u_x)^{\frac{3}{2}}} - \lambda(u - I_{BM3D}) \right).$$

with symmetric boundary conditions:

$$\begin{aligned} u_{-1,j}^k &= u_{0,j}^k, & u_{M+1,j}^k &= u_{M,j}^k, & j &= 0, 1, \dots, N. \\ u_{i,-1}^k &= u_{i,0}^k, & u_{i,N+1}^k &= u_{i,N}^k, & i &= 0, 1, \dots, M. \end{aligned}$$

where  $M \times N$  is the image size.

### III. EXPERIMENTS RESULTS AND ANALYSIS

Fig. 3(a) displays the computer simulated Shepp-Logan head phantom composed of 256 pixels  $\times$  256 pixels. Fig. 3(b) illustrates the computer simulated pelvis phantom with 252 pixels  $\times$  256 pixels. Fig. 3(d) and Fig. 3(e) corresponding to Fig. 3(a) and Fig. 3(b) show the LDCT images obtained by performing the FBP reconstruction using low-pass Hanning filter with cutoff at 80% Nyquist frequency from simulated noisy sonogram. In addition, the thoracic phantom,

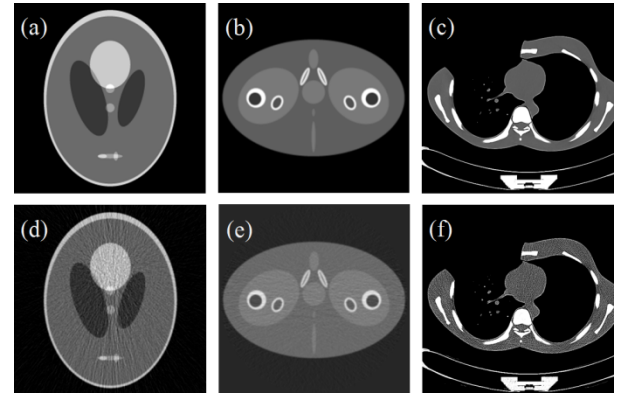


**FIGURE 3. Simulative phantoms and actual images. (a) original Shepp-Logan head phantom; (b) original pelvis phantom; (c) processed HDCT thoracic image by AS-LNLM method; (d)-(e) LDCT images corresponding to (a) and (b); (f) LDCT thoracic image corresponding to (c).**

an anatomical model of a human chest torso, is also used in our experiment, and it is collected from a multi-detector row Siemens Somatom Sensation 16 CT scanner with a tube voltage of 120 kVp. The original thoracic high-dose computed tomography (HDCT) image is collected with a higher tube current of 240 mAs. Fig. 3(c) shows the processed HDCT image using the AS-LNLM (Artifact Suppressed Large-scale Nonlocal Means) method. In [37], the processed HDCT image by AS-LNLM method has a better noise and artifact suppression than the original HDCT images, so it is used as the reference HDCT image. Both original thoracic LDCT phantom and processed LDCT thoracic phantom are the 16th slice of the volume in a mediastinal window. Fig. 3(f) displays the original LDCT image obtained with a reduced tube current 30mAs. Fig. 3(c), Fig. 3(f) are composed of 512 pixels  $\times$  512 pixels.

#### A. OBJECTIVE EVALUATION CRITERIA

In order to evaluate the effectiveness of the processed NTV model, the peak signal-to-noise ratio (PSNR) and the mean structural similarity (MSSIM) [38] are employed as objective indices to measure the quality of restoration results.

For a reference HDCT image  $X$  and the restored LDCT image  $Y$ , PSNR is described in dB, which is defined with:

$$PSNR = 10 \cdot \lg \left( \frac{255^2}{MSE} \right),$$

where,

$$MSE = \frac{1}{MN} \sum_{i=1}^{MN} (X_i - Y_i)^2,$$

$M \times N$  is the size of image  $X$  and  $Y$ . A higher PSNR indicates the restoration with higher quality and less distortion.

Another evaluation criterion is MSSIM, which is used to measure the overall structural similarity between  $X$  and  $Y$ :

$$MSSIM(X, Y) = \frac{1}{T} \sum_{j=1}^T SSIM(x_j - y_j),$$

where,  $x_j$  and  $y_j$  are the image blocks of size  $k \times k$  at  $j$ th local window in  $X$  and  $Y$ , and  $T$  is the amount of local windows in the image. SSIM measures the structural similarity between  $x_j$  and  $y_j$ :

$$SSIM(x_j, y_j) = \frac{(2\mu_{x_j}\mu_{y_j} + c_1)(2cov(x_j, y_j) + c_2)}{(\mu_{x_j}^2 + \mu_{y_j}^2 + c_1)(\sigma_{x_j}^2 + \sigma_{y_j}^2 + c_2)},$$

where,

$$\mu_{x_j} = \frac{1}{k^2} \sum_{i=1}^{k^2} x_{ji}, \quad \sigma_{x_j}^2 = \frac{1}{k^2 - 1} \sum_{i=1}^{k^2} (x_{ji} - \mu_{x_j})^2,$$

$$\mu_{y_j} = \frac{1}{k^2} \sum_{i=1}^{k^2} y_{ji}, \quad \sigma_{y_j}^2 = \frac{1}{k^2 - 1} \sum_{i=1}^{k^2} (y_{ji} - \mu_{y_j})^2,$$

$$cov(x_j, y_j) = \frac{1}{k^2 - 1} (x_j - \mu_{x_j})(y_j - \mu_{y_j}),$$

where  $\mu_{x_j}$  is the average of  $x_j$ ,  $\mu_{y_j}$  is the average of  $y_j$ ,  $\sigma_{x_j}^2$  is the variance of  $x_j$ ,  $\sigma_{y_j}^2$  is the variance of  $y_j$ , is the covariance between  $x_j$  and  $y_j$ ,  $c_1$  and  $c_2$  are positive constant.

MSSIM is able to measure the structural information preservation, and its value locates in  $[0, 1]$ . Better preservation of structural information results in higher MSSIM. MSSIM value closing to 1 implies that the original image structural information is well preserved, i.e.,  $X$  is equal to  $Y$  approximately. In contrast, MSSIM value closing to 0 implies that the two images are almost irrelevant.

**B. PARAMETER ANALYSIS**

To evaluate the efficiency and feasibility of the proposed NTV image restoration method in this paper, several methods including modified Perona-Malik (MPM) [39], MTV [28], FPMTV [22], K-Singular Value Decomposition (K-SVD) [40], improved non-local means (INLM) [41], BM3D [29] and weighted nuclear norm minimization (WNNM) [42] are served as the comparative methods to process LDCT images. The parameters involved in MPM, MTV, FPMTV, K-SVD, INLM, BM3D and WNNM are set according to the suggestions in [22], [28], [29], and [39]–[42]. The parameters in NTV are given under the optimal visual effects and the best objective evaluation criteria, and for all LDCT images processed by NTV, we choose: and the Gaussian filter with the deviation of 0.5. Iteration stops when MSSIM reaches maximum.

The parameter  $\lambda$  and  $k$  are decided by MSSIM, PSNR and the visual effect of the denoised LDCT Shepp-Logan image. Fig. 4(a) shows the MSSIM value of NTV model with different  $\lambda$  between 0.01 and 1.0 with time interval 0.2. As we can see from Fig. 4(a), the MSSIM of the NTV model with  $\lambda = 1.0$  increases quickly and then reaches maximum while the MSSIM with smaller  $\lambda$  converge to the similar-valued maximum more slowly, which indicates that  $\lambda = 1.0$  leads to lower computing cost with similar maximum MSSIM value. But from Fig. 4(b), at the same  $k$ , the PSNR value of NTV with  $\lambda = 0.5$  is higher than that with  $\lambda = 1.0$ , so at last we choose  $\lambda = 0.5$  in the NTV model.

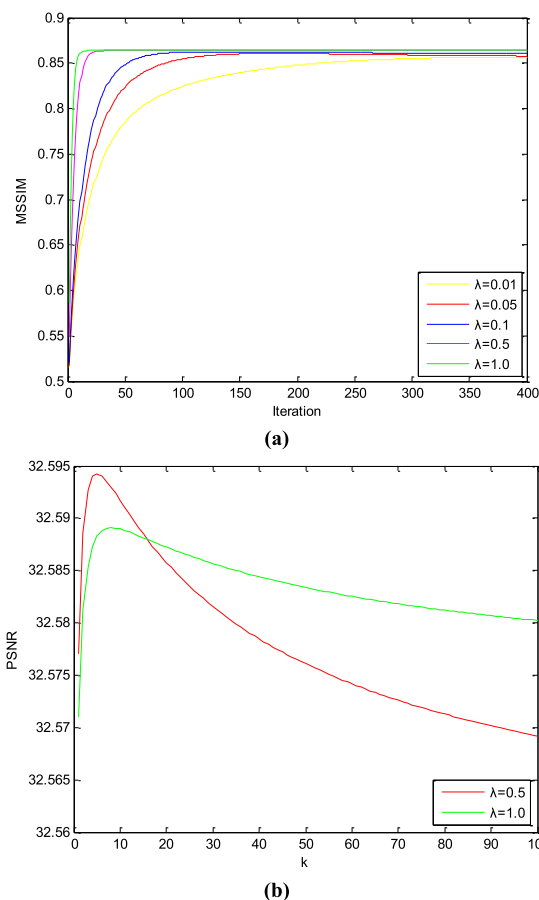


**FIGURE 4. (a) The MSSIM of the NTV model with different; Fig. 4 (b) The PSNR of the NTV model with different.**

**TABLE 2. Parameter settings of the proposed NTV method for computer simulated phantom and actual thoracic phantom.**

	$dt$	$\lambda$	$\sigma$	$iter$	$k$
Shepp-Logan head phantom	0.2	0.5	0.5	32	6
pelvis phantom	0.2	0.5	0.5	66	1
thoracic phantom	0.5	0.5	0.5	31	300

In addition, in this paper, we set  $k = 6$ ,  $k = 1$  and  $k = 300$  for the Shepp-Logan head phantom, the pelvis phantom and the thoracic phantom in the NTV model respectively. In order to intuitively illustrate the values of parameters in NTV method, we give them in Table 2.

**C. EXPERIMENTAL RESULTS**

**1) THE SHEPP-LOGAN HEAD PHANTOM AND THE PELVIS PHANTOM**

Fig. 5 and Fig. 6 are the Shepp-Logan head phantom and the pelvis phantom respectively. More specifically, Fig. 5(a) and Fig. 6(a) are the original Shepp-Logan head phantom and the original pelvis phantom. Fig. 5(b) and Fig. 6(b) show the corresponding LDCT images.

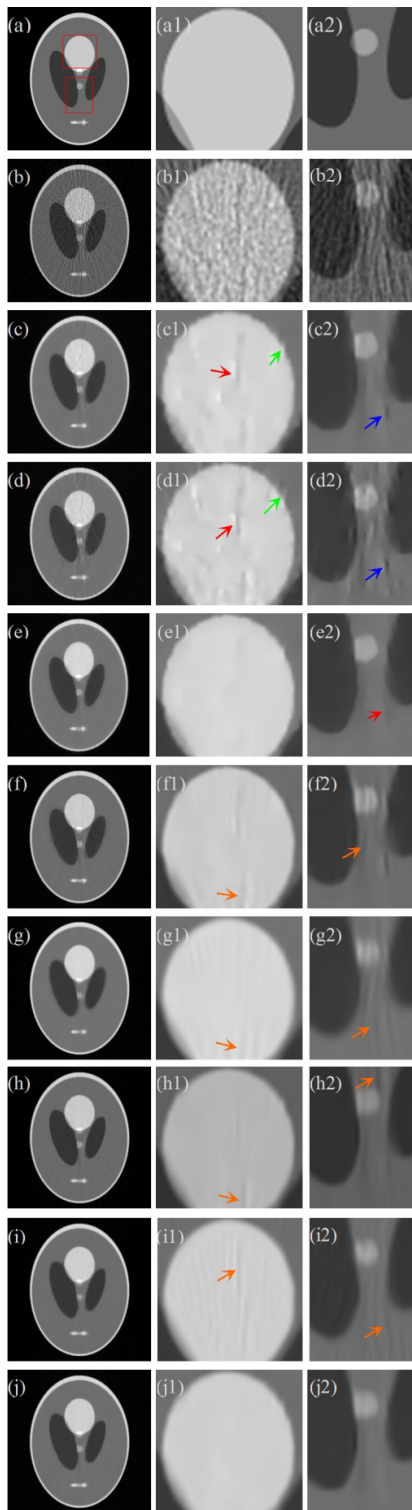


**FIGURE 5.** Comparative experiments on the Shepp-Logan head phantom. (a) original phantom; (b) LDCT image; (c) processed image by MPM method; (d) processed image by MTV method; (e) processed image by FPMTV method; (f) processed image by K-SVD method; (g) processed image by INLM method; (h) processed image by BM3D method; (i) processed image by WNNM method; and (j) processed image by NTV method. From left to right, the images in the second and third columns show the zoomed ROIs specified in (a), and all of the zoomed images are from the corresponding images of the first column.

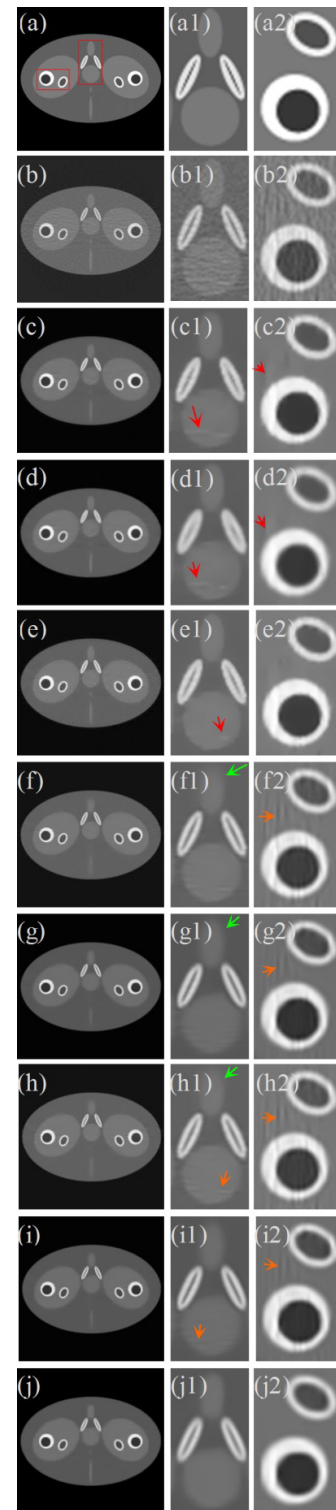


**FIGURE 6.** Comparative experiments on the pelvis phantom. (a) original phantom; (b) LDCT image; (c) processed image by MPM method; (d) processed image by MTV method; (e) processed image by FPMTV method; (f) processed image by K-SVD method; (g) processed image by INLM method; (h) processed image by BM3D method; (i) processed image by WNNM method; and (j) processed image by NTV method; From left to right, the images in the second and third columns show the zoomed ROIs specified in (a), and all of the zoomed images are from the corresponding images of the first column.

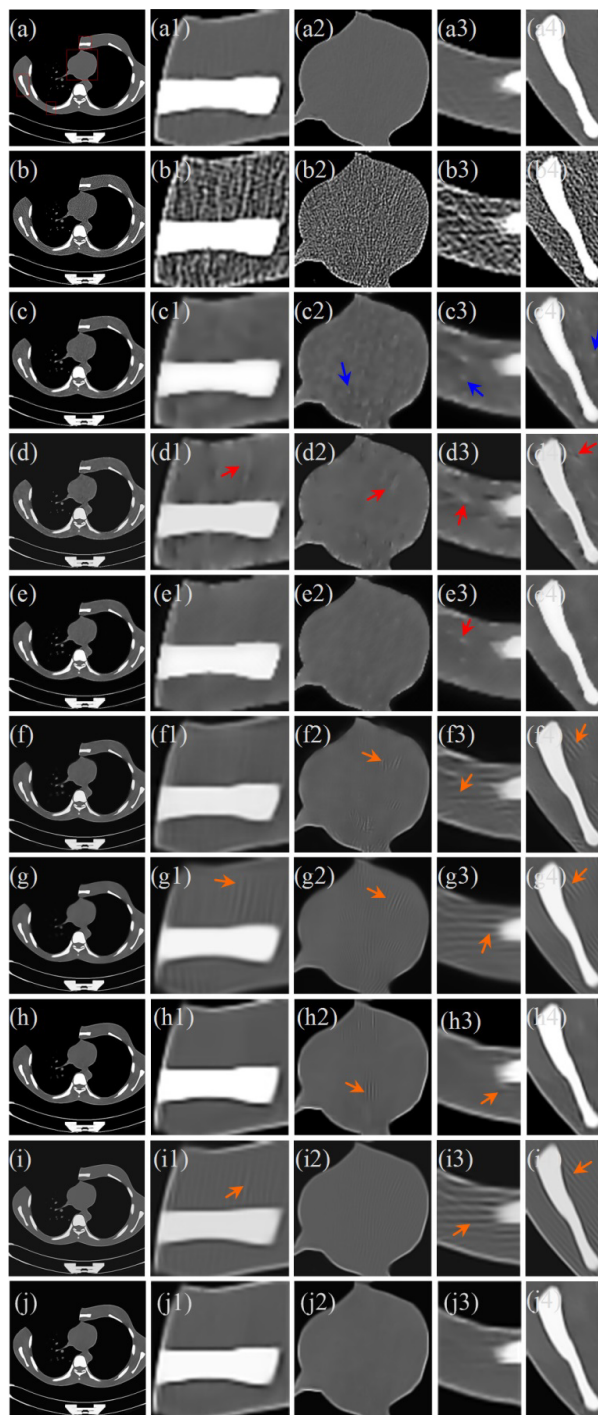


**FIGURE 7.** Comparative experiments on the actual thoracic phantom. (a) processed HDCT image by AS-LNLM method; (b) LDCT image; (c) processed image by MPM method; (d) processed image by MTV method; (e) processed image by FPMTV method; (f) processed image by K-SVD method; (g) processed image by INLM method; (h) processed image by BM3D method; (i) processed image by WNNM method; and (j) processed image by NTV method; From left to right, the images in the columns 2-5 show the zoomed ROIs specified in (a), and all of the zoomed images are from the corresponding images of the first column.

Fig. 5-Fig. 6, (c)-(j) show the MPM processed LDCT images, MTV processed LDCT images, FPMTV processed LDCT images, K-SVD processed LDCT images, INLM

**TABLE 3.** Objective evaluation criteria of various restoration algorithms.

Image	Method	PSNR(dB)	MSSIM
Shepp-Logan head phantom	MPM	21.6819	0.5519
	MTV	20.8211	0.5593
	FPMTV	21.7274	0.5560
	K-SVD	22.9443	0.5630
	INLM	22.2476	0.5613
	BM3D	32.5395	0.8646
	WNNM	22.9184	0.5336
	NTV	32.5168	0.8637
pelvis phantom	MPM	23.5986	0.9053
	MTV	21.5544	0.9051
	FPMTV	24.2124	0.8817
	K-SVD	23.7804	0.8900
	INLM	23.9446	0.9192
	BM3D	30.0305	0.9761
	WNNM	24.9672	0.9292
	NTV	30.2294	0.9734
thoracic phantom	MPM	26.2685	0.9220
	MTV	26.4869	0.9365
	FPMTV	26.5195	0.8802
	K-SVD	27.3768	0.9186
	INLM	26.4852	0.9264
	BM3D	26.9899	0.9524
	WNNM	27.0358	0.9443
	NTV	26.9967	0.9532

processed LDCT images, BM3D processed LDCT images, WNNM processed LDCT images and NTV processed LDCT images respectively. To study experiment results of these comparative methods in depth, the zoomed regions of interest (ROI) identified by red squares in (a) are illustrated in Fig. 5-6, (a1)-(j1) and (a2)-(j2). From Fig. 5(b) and Fig. 6(b), we can see that mottle noise and streak artifacts severely degrade the images reconstructed under low dose CT scanning condition. From (c) of Fig. 5 and Fig. 6, we know that MPM method suffers from the blocky effect (pointed by red arrows), tends to blur edges (pointed by green arrows), and contains residual mottle noise and streak artifacts (shown by blue arrows). Fig. 5(d)-6(d) processed by MTV method also give rise to the blocky effect as well as the blurry edges, and there are still some residual mottle noise and streak artifacts. The denoised LDCT images processed from the FPMTV method are shown in Fig. 5(e)-6(e), in which the blocky effect still exists (pointed by red arrows). We can clearly see that Fig. 5(f)-6(f) processed by K-SVD method, Fig. 5(g)-6(g) processed by INLM method, Fig. 5(h)-6(h) processed by BM3D method and Fig. 5(i)-6(i) processed by WNNM method perform better than those processed by MPM method and by MTV method in mottle noise and streak

**TABLE 4.** PSNR and MSSIM of three ROIs (corresponding to rectangular boxes marked with a red line of the under Shepp-Logan head phantom ) of processed images using MPM, MTV, FPMTV, K-SVD, INLM, BM3D, WNNM and NTV.

	ROI1		ROI2		ROI3	
	PSNR	MSSIM	PSNR	MSSIM	PSNR	MSSIM
LDCT image	13.4347	0.0145	12.1504	0.0155	12.1333	0.0175
MPM	26.4979	0.3229	25.5528	0.2588	21.9571	0.3403
MTV	21.2980	0.1062	21.0594	0.1387	18.5380	0.1682
FPMTV	34.4731	0.8794	32.4888	0.7011	25.5366	0.6397
K-SVD	33.0705	0.6662	26.2197	0.3903	22.8642	0.3467
INLM	34.9728	0.7034	29.0126	0.4752	25.7026	0.4175
BM3D	41.3022	0.9798	35.6162	0.7791	33.0014	0.9051
WNNM	29.4389	0.4933	30.8438	0.4588	26.9184	0.4460
NTV	45.8389	0.9959	35.7142	0.9895	34.4892	0.9331

**TABLE 5.** PSNR and MSSIM of four ROIs (corresponding to rectangular boxes marked with a red line of the under the actual thoracic phantom ) of processed images using MPM, MTV, FPMTV, K-SVD, INLM, BM3D, WNNM and NTV.

	ROI1		ROI2		ROI3		ROI4	
	PSNR	MSSIM	PSNR	MSSIM	PSNR	MSSIM	PSNR	MSSIM
LDCT image	13.2379	0.0120	13.0254	0.0248	12.6163	0.0351	13.0342	0.0209
MPM	29.5269	0.7498	27.8606	0.7274	31.3831	0.5972	30.9283	0.7435
MTV	28.6396	0.8156	26.8138	0.6777	30.1899	0.6463	31.3440	0.8273
FPMTV	32.4425	0.8915	30.3642	0.8876	32.9581	0.6196	32.3402	0.8851
K-SVD	28.9068	0.3949	27.1623	0.3793	25.2747	0.2735	27.3632	0.4379
INLM	29.6504	0.5867	29.7829	0.7221	31.5270	0.6701	29.7626	0.6292
BM3D	30.9387	0.9361	29.3206	0.9271	34.9992	0.8229	32.8283	0.7909
WNNM	31.8032	0.7772	33.4873	0.8869	27.8779	0.5562	28.2699	0.7475
NTV	32.9887	0.9584	29.8445	0.9404	34.7007	0.8633	33.4751	0.9098

artifacts suppression, but introduce new artifacts (shown by orange arrows). The problem of edges blurring also can be seen in Fig. 6(f)-(h). Comparing with the result images processed by the other methods, Fig. 5(j)-6(j) processed by the proposed NTV method indicate that NTV has better performance in edges and details preservation and outstanding mottle noise and streak artifacts suppression ability.

## 2) THE ACTUAL THORACIC PHANTOM

The actual thoracic phantom is shown in Fig. 7. Fig. 7(a) is the processed thoracic HDCT image by AS-LNLM method.

Fig. 3 (f) shows the LDCT image obtained with a reduced tube current of 30 mAs. In order to accurately compare the result images of various algorithms, four zoomed images of local regions marked by red boxes in Fig. 7(a) are also shown in Fig. 7(a1)-(j1), (a2)-(j2), (a3)-(j3) and (a4)-(j4). Mottle noise and streak artifacts can be easily observed in the original thoracic LDCT image, i.e., Fig. 7(b). Fig. 7(j) is the restored image by the proposed NTV method. We can observe that streak artifacts are suppressed effectively and image quality obtains significant improvement. The reconstructed images by the MPM algorithm are shown in Figs. 7(c), in which

**TABLE 6. Computation time (in seconds) for different methods.**

	MPM	MTV	FPMTV	K-SVD	INLM	BM3D	WNNM	NTV
Shepp phantom	20.90	18.74	10.12	72.98	7.62	0.9	570.33	1.36
plevis phantom	15.13	20.63	6.38	121.68	7.11	0.8	493.05	3.01
Thoracic phantom	50.39	49.39	29.62	56.85	63.48	3.9	394.70	4.88

there are still some residual mottle noise and streak artifacts (pointed by blue arrows). Figs. 7(d) and Fig. 7(e) illustrate that the processed images by the MTV method and by the FPMTV model suffer from obvious blocky effect (pointed by red arrows). Additionally, from Fig. 7(f), Fig. 7(g), Fig. 7(h) and Fig. 7(i) processed images by the K-SVD method, by the INLM method, by the BM3D method and by the WNNM method respectively, we know that they tend to cause new and residual streak artifacts (shown by orange arrows).

The objective evaluation criteria PSNR and MSSIM listed in TABLE 3 indicate that the proposed NTV model and the BM3D model are almost identical, and they are superior to other comparative models. Moreover, the result images in Fig. 5-7 show that NTV model has better visual effect than all the comparative models, including BM3D. That is to say, the effectiveness of new model is testified by both quantitative analysis and visual effect.

In order to go deep into experimental results, in TABLE 4, we list the PSNR and the MSSIM of three ROIs (corresponding to the red rectangular boxes of the Shepp-Logan head phantom in TABLE 4) of processed images using MPM, MTV, FPMTV, K-SVD, INLM, BM3D, WNNM and NTV separately. In the same way, TABLE 5 shows the PSNR and the MSSIM of four ROIs (corresponding to the red rectangular boxes of the actual thoracic phantom in TABLE 5) of processed image using MPM, MTV, FPMTV, K-SVD, INLM, BM3D, WNNM and NTV respectively.

From TABLE 4, TABLE 5, we know that the processed LDCT images by NTV method generally have higher PSNR and MSSIM than the other restoration methods.

### 3) COMPUTATION COSTS

All experiments are simulated on a PC with Intel(R) Pentium(R) CPU 2.90 GHz and 4GB RAM using the MATLAB 2012a language.

TABLE 6 lists the computation time for eight different methods (i.e., MPM, MTV, FPMTV, K-SVD, INLM, BM3D, WNNM and NTV method). We can see that the proposed NTV method and the BM3D model take less time than the other methods.

## IV. CONCLUSION

This paper proposes a post-processing model (NTV) for LDCT images restoration. In the NTV model, the weighted coefficient of the regularization term is constructed depend-

ing on standard deviation, gray-level probability and gradient magnitude, because they can differentiate edges and detail information from the noisy background effectively, which makes the NTV model achieve a stronger diffusion in noisy background than that in detail region and edges. In addition, to preserve image structure effectively, the processed LDCT images by BM3D filter are used in the fidelity item of the NTV model instead of the processed LDCT images by Gaussian filter of the MTV model.

Experiments are implemented on the computer simulated phantom and the actual phantom. Both subjective visual effects and objective evaluation criteria show that the LDCT images processed by NTV model have significant quality improvement, including mottle noise, streak artifacts and blocky effect suppression, edges and details preservation, and the relative lower calculate cost. Besides, since the proposed NTV method does not rely on raw projection data directly, NTV can be easily applied to almost all the existing CT systems.

However, some artifacts still exist in the processed LDCT images by NTV model. In fact, this is a common issue in post-processing since noise already exists in the raw projection data. In this case, in the further, projection data preprocessing strategies might be required to alleviate artifacts of the raw projection data, then the processed projection data is used for the proposed NTV method.

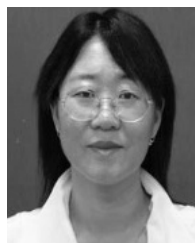
## REFERENCES

- [1] Y. Chen et al., "Improving abdomen tumor low-dose CT images using a fast dictionary learning based processing," *Phys. Med. Biol.*, vol. 58, pp. 5803–5820, Aug. 2013.
- [2] R. Smith-Bindman et al., "Radiation dose associated with common computed tomography examinations and the associated lifetime attributable risk of cancer," *Arch. Int. Med.*, vol. 169, no. 22, pp. 2078–2086, 2009.
- [3] M. K. Kalra et al., "Strategies for CT radiation dose optimization," *Radiology*, vol. 230, no. 3, pp. 619–628, Mar. 2004.
- [4] M. Yazdi and L. Beaulieu, "Artifacts in spiral X-ray CT scanners: Problems and solutions," *Int. J. Biol. Med. Sci.*, vol. 4, no. 3, pp. 135–139, 2008.
- [5] J. Wang, H. Lu, J. Wen, and Z. Liang, "Multiscale penalized weighted least-squares sinogram restoration for low-dose X-ray computed tomography," *IEEE Trans. Biomed. Eng.*, vol. 55, no. 3, pp. 1022–1031, Mar. 2008.
- [6] E. C. Ehman et al., "Noise reduction to decrease radiation dose and improve conspicuity of hepatic lesions at contrast-enhanced 80-kV hepatic CT using projection space denoising," *AJR*, vol. 198, no. 2, pp. 405–411, 2012.
- [7] Y. Liu and Z.-G. Gui, "A statistical iteration approach with energy minimization to sinogram noise reduction for low-dose X-ray CT," *Optik*, vol. 123, no. 23, pp. 2174–2178, 2012.

- [8] Y. Liu, Z. Gui, and Q. Zhang, "Noise reduction for low-dose X-ray CT based on fuzzy logical in stationary wavelet domain," *Opt. Int. J. Light Electron*, vol. 124, no. 18, pp. 3348–3352, 2013.
- [9] S. Z. Niu, H. Wu, Z. F. Yu, Z. J. Zheng, and G. H. Yu, "Total generalized variation minimization based on projection data for low-dose CT reconstruction," *J. Southern Med. Univ.*, vol. 37, no. 12, pp. 1585–1591, 2017.
- [10] E. Y. Sidky and X. Pan, "Image reconstruction in circular cone-beam computed tomography by constrained, total-variation minimization," *Phys. Med. Biol.*, vol. 53, no. 17, pp. 4777–4807, 2008.
- [11] Y. Liu, H. Shangguan, Q. Zhang, H. Zhu, H. Shu, and Z. Gui, "Median prior constrained TV algorithm for sparse view low-dose CT reconstruction," *Comput. Biol. Med.*, vol. 60, pp. 117–131, May 2015.
- [12] Y. Chen, J. Ma, Q. Feng, L. Luo, P. Shi, and W. Chen, "Nonlocal prior Bayesian tomographic reconstruction," *J. Math. Imag. Vis.*, vol. 30, no. 2, pp. 133–146, 2008.
- [13] Y. Chen et al., "Bayesian statistical reconstruction for low-dose X-ray computed tomography using an adaptive-weighting nonlocal prior," *Comput. Med. Imag. Graph.*, vol. 33, no. 7, pp. 495–500, 2009.
- [14] M. G. Lubner, P. J. Pickhardt, J. Tang, and G.-H. Chen, "Reduced image noise at low-dose multidetector CT of the abdomen with prior image constrained compressed sensing algorithm," *Radiology*, vol. 260, no. 1, pp. 248–256, 2011.
- [15] Q. Liu, M. Zhang, and J. Zhao, "Adaptive dictionary learning in sparse gradient domain for CT reconstruction," *IEEE Trans. Image Process.*, vol. 22, no. 12, pp. 4652–4663, Dec. 2013.
- [16] J. C. R. Giraldo et al., "Comparative study of two image space noise reduction methods for computed tomography: Bilateral filter and nonlocal means," in *Proc. Annu. Int. Conf. IEEE Eng. Med. Biol. Soc.*, Minneapolis, MN, USA, Sep. 2009, pp. 3529–3532.
- [17] Y. Chen et al., "Improving low-dose abdominal CT images by weighted intensity averaging over large-scale neighborhoods," *Eur. J. Radiol.*, vol. 80, no. 2, pp. e42–e49, 2011.
- [18] Y. Chen et al., "Thoracic low-dose CT image processing using an artifact suppressed large-scale nonlocal means," *Phys. Med. Biol.*, vol. 57, no. 9, pp. 2667–2688, 2012.
- [19] Y. Chen et al., "Artifact suppressed dictionary learning for low-dose CT image processing," *IEEE Trans. Med. Imag.*, vol. 33, no. 12, pp. 2271–2292, Dec. 2014.
- [20] H. Chen et al., "Low-dose CT via convolutional neural network," *Biomed. Opt. Express*, vol. 8, no. 2, pp. 679–694, 2017.
- [21] Y. Liu, M. Castro, M. Lederlin, H. Shu, A. Kaladji, and P. Haigron, "Edge-preserving denoising for intra-operative cone beam CT in endovascular aneurysm repair," *Comput. Med. Imag. Graph.*, vol. 56, pp. 49–59, Mar. 2017.
- [22] Y. Wang, Y. Shao, Z. Gui, Q. Zhang, L. Yao, and Y. Liu, "A novel fractional-order differentiation model for low-dose CT image processing," *IEEE Access*, vol. 4, pp. 8487–8499, 2016.
- [23] P. Perona and J. Malik, "Scale-space and edge detection using anisotropic diffusion," *IEEE Trans. Pattern Anal. Mach. Intell.*, vol. 12, no. 7, pp. 629–639, Jul. 1990.
- [24] L. I. Rudin, S. Osher, and E. Fatemi, "Nonlinear total variation based noise removal algorithms," *Phys. D, Nonlinear Phenomena*, vol. 60, nos. 1–4, pp. 259–268, 1992.
- [25] Y.-L. You and M. Kaveh, "Fourth-order partial differential equations for noise removal," *IEEE Trans. Image Process.*, vol. 9, no. 10, pp. 1723–1730, Oct. 2000.
- [26] M. Lysaker and X.-C. Tai, "Iterative image restoration combining total variation minimization and a second-order functional," *Int. J. Comput. Vis.*, vol. 66, no. 1, pp. 5–18, 2006.
- [27] M. R. Hajiaboli, "An anisotropic fourth-order diffusion filter for image noise removal," *Int. J. Comput. Vis.*, vol. 92, no. 2, pp. 177–191, 2011.
- [28] Y. Wang, W. Chen, S. Zhou, T. Yu, and Y. Zhang, "MTV: modified total variation model for image noise removal," *Electron. Lett.*, vol. 47, no. 10, pp. 592–594, May 2011.
- [29] K. Dabov, A. Foi, V. Katkovnik, and K. Egiazarian, "Image denoising by sparse 3-D transform-domain collaborative filtering," *IEEE Trans. Image Process.*, vol. 16, no. 8, pp. 2080–2095, Aug. 2007.
- [30] L. C. Evans and R. F. Gariepy, *Measure Theory and Fine Properties of Functions*. Boca Raton, FL, USA: CRC Press, 1992.
- [31] E. Giusti, *Minimal Surfaces and Functions of Bounded Variation* (Monographs in Mathematics), vol. 80. Basel, Switzerland: Birkhäuser Verlag, 1984.
- [32] Y. Chen and T. Wunderli, "Adaptive total variation for image restoration in BV space," *J. Math. Anal. Appl.*, vol. 272, no. 1, pp. 117–137, 2002.
- [33] Y. Chen and M. Rao, "Minimization problems and associated flows related to weighted  $p$  energy and total variation," *SIAM J. Math. Anal.*, vol. 34, no. 5, pp. 1084–1104, 2006.
- [34] M. Malarvel, G. Sethumadhavan, P. C. R. Bhagi, S. Kar, T. Saravanan, and A. Krishnan, "Anisotropic diffusion based denoising on X-radiography images to detect weld defects," *Digit. Signal Process.*, vol. 68, pp. 112–126, Sep. 2017.
- [35] S.-M. Chao and D.-M. Tsai, "An improved anisotropic diffusion model for detail- and edge-preserving smoothing," *Pattern Recognit. Lett.*, vol. 31, no. 13, pp. 2012–2023, 2010.
- [36] M. Lysaker and X.-C. Tai, "Iterative image restoration combining total variation minimization and a second-order functional," *Int. J. Comput. Vis.*, vol. 66, no. 1, pp. 5–18, 2006.
- [37] Y. Chen et al., "Thoracic low-dose CT image processing using an artifact suppressed large-scale nonlocal means," *Phys. Med. Biol.*, vol. 57, no. 9, pp. 2667–2688, 2012.
- [38] Z. Wang, A. C. Bovik, H. R. Sheikh, and E. P. Simoncelli, "Image quality assessment: From error visibility to structural similarity," *IEEE Trans. Image Process.*, vol. 13, no. 4, pp. 600–612, Apr. 2004.
- [39] Y. Q. Wang, J. Guo, W. Chen, and W. Zhang, "Image denoising using modified Perona–Malik model based on directional Laplacian," *Signal Process*, vol. 93, no. 9, pp. 2548–2558, 2013.
- [40] M. Aharon, M. Elad, and A. Bruckstein, "K-SVD: An algorithm for designing overcomplete dictionaries for sparse representation," *IEEE Trans. Signal Process.*, vol. 54, no. 11, pp. 4311–4322, Nov. 2006.
- [41] B. Goossens, H. Luong, A. Pizurica, and W. Philips, "An improved non-local denoising algorithm," in *Proc. LNLA*, Lausanne, Switzerland, 2008, pp. 143–156.
- [42] S. Gu, L. Zhang, W. Zuo, and X. Feng, "Weighted nuclear norm minimization with application to image denoising," in *Proc. IEEE Conf. Comput. Vis. Pattern Recognit.*, Jun. 2014, pp. 2862–2869.



**WENBIN CHEN** is currently pursuing the Ph.D. degree in signal and information processing with the North University of China. Her research interests are in image processing with partial differential equation and CT imaging reconstruction.



**YANLING SHAO** received the Ph.D. degree in mathematics from the Beijing Institute of Technology, in 2005. She joined the Department of Mathematics, North University of China, in 1983, where she is currently a Professor. She has authored over one hundred scientific publications. Her primary research interests include matrix theory and graph theory.



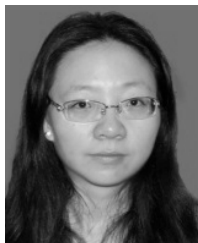
**YANLING WANG** received the Ph.D. degree in signal and information processing from the North University of China, in 2018. She joined the School of Information Management, Shanxi University of Finance and Economics, in 2018. Her research interests include image processing and CT imaging reconstruction.



**QUAN ZHANG** received the Ph.D. degree in computer science and technology from Southeast University, in 2014. He is currently engages in teaching and research work as an Associate Professor with the North University of China. His research interests include medical imaging reconstruction and medical image analysis.



**YAN CHEN** received the Ph.D. degree in signal and information processing from the North University of China, in 2016, where she joined the School of Information and Communication Engineering, in 2004. Her research interests include image processing and reconstruction.



**YI LIU** received the Ph.D. degree in signal and information processing from the North University of China, in 2014. She joined the School of Information and Communication Engineering, North University of China, in 2015. Her research interests include CT imaging and image processing.



**GUANRU YANG** is currently pursuing the graduate degree in electronic information engineering with the Faculty of Information Technology, Beijing University of Technology. His research interests include signal and information processing, and image processing and recognition.



**LINHONG YAO** received the Ph.D. degree in fundamental mathematics from Beijing Normal University, in 2012. She joined the College of Science, North University of China. Her research interests include partial differential equations, nonlinear analysis, and mathematical method in image processing.



**ZHIGUO GUI** received the Ph.D. degree in signal and information processing from the North University of China, in 2004. He is currently a Professor with the North University of China. His research interests include signal and information processing, image processing and recognition, and image reconstruction.

...